JACS
JOURNAL OF THE AMERICAN CHEMICAL SOCIETY
Article
pubs.acs.org/JACS

# Complex and Noncentrosymmetric Stacking of Layered Metal Dichalcogenide Materials Created by Screw Dislocations

Melinda J. Shearer,[†] Leith Samad,[†] Yi Zhang,[†] Yuzhou Zhao,[†] Alexander Puretzky,[‡] Kevin W. Eliceiri,[§] John C. Wright,[†] Robert J. Hamers,*[,†] and Song Jin*[,†]

[†]Department of Chemistry, University of Wisconsin−Madison, Madison, Wisconsin 53706, United States
[‡]Center for Nanophase Materials Sciences, Oak Ridge National Laboratory, Oak Ridge, Tennessee 37831, United States
[§]Laboratory for Optical and Computational Instrumentation, University of Wisconsin−Madison, Madison, Wisconsin 53706, United States

Supporting Information

**ABSTRACT:** The interesting and tunable properties of layered metal dichalcogenides heavily depend on their phase and layer stacking. Here, we show and explain how the layer stacking and physical properties of $WSe_2$ are influenced by screw dislocations. A one-to-one correlation of atomic force microscopy and high- and low-frequency Raman spectroscopy of many dislocated $WSe_2$ nanoplates reveals variations in the number and shapes of dislocation spirals and different layer stackings that are determined by the number, rotation, and location of the dislocations. Plates with triangular dislocation spirals form noncentrosymmetric stacking that gives rise to strong second-harmonic generation and enhanced photoluminescence, plates with hexagonal dislocation spirals form the bulk 2H layer stacking commonly observed, and plates containing mixed dislocation shapes have intermediate noncentrosymmetric stackings with mixed properties. Multiple dislocation cores and other complexities can lead to more complex stackings and properties. These previously unobserved properties and layer stackings in $WSe_2$ will be interesting for spintronics and valleytronics.

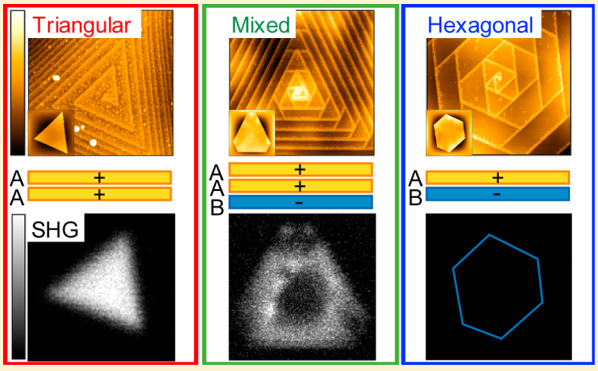


## INTRODUCTION

Layered transition metal dichalcogenides ($MX_2$), such as $MoS_2$ and $WSe_2$, are fascinating two-dimensional (2D) materials for a variety of applications, including optoelectronics,[1] spintronics,[2,3] valleytronics,[2,4,5] and catalysis.[6,7] Such diverse applications are accessible in part because the properties of $MX_2$ materials can be tuned via many processes, such as thinning to few-layer (<6L),[8,9] application of strain,[10] or perhaps most notably by changing the phase and layer stacking.[11−15] Typically, group VI $MX_2$ materials (M = Mo, W) are synthesized and studied in the thermodynamically stable phase at ambient conditions, the centrosymmetric hexagonal 2H phase, which has two repeating layers each made of $MX_6$ units with trigonal prismatic metal coordination. Other phases have been shown to have unique properties for specific applications, such as the enhanced catalytic activity for hydrogen evolution shown by the 1T phase[6,12,16] and utility in spintronics and valleytronics for the rare 3R phase.[2,5] The 3R phase, which has been reported for some Group VI $MX_2$ materials,[11,17] differs from the 2H phase only in the stacking and orientation of the layers (ABC vs AB layer stacking), but this seemingly small change has huge implications, as the 3R phase is noncentrosymmetric. Thus, changes in the stacking alone can greatly influence the properties and applications of $MX_2$ materials.[11]

A unique attribute of 2D materials is that individual layers can be stacked to create complex forms of atomically controlled artificial materials.[18] One method for achieving this structural complexity in few-layer structures is by changing the orientation of individual layers, either through direct chemical vapor deposition (CVD) growth[14,19] or mechanical stacking of exfoliated[20] or CVD grown[21−23] layers. The resulting changes in layer stacking can be studied using low-frequency (LF) Raman,[14,21,24] second-harmonic generation (SHG),[19,20,23] and other spectroscopic techniques.[19,20,22] Additionally, vertical heterostructures, which have at least two different $MX_2$ materials stacked on top of each other, are another form of artificial 2D materials with complex stacking that have shown new properties interesting for optoelectronics.[25−28] Manipulation of layer stackings at the few-layer level has been well-studied; however, thus far there has been little understanding on how to access diverse layer stackings over many layers within the same $MX_2$ material.

**Received:** December 9, 2016
**Published:** February 8, 2017




DOI: 10.1021/jacs.6b12559
J. Am. Chem. Soc. 2017, 139, 3496−3504

The growth of $MX_2$ materials as well as other layered materials, such as $Bi_2Se_3$ and layered metal hydroxides, can be readily driven by screw dislocations.[29−35] Screw dislocations can drive the anisotropic growth of a variety of one-dimensional (1D) and 2D nanomaterials.[36,37] For layered materials, the inclusion of a screw dislocation is an interesting concept as a screw dislocation is a singularity in space that connects different layers of the 2D crystal structure in a continuous spiral, which can create additional complexity in layer stackings beyond the few-layer level. However, there has been little work on systematically understanding the effects of screw dislocations on the nanostructure and layer stacking of $MX_2$ materials, which is critical for understanding their emerging properties. In this paper, we experimentally reveal how screw dislocations can greatly influence the growth and layer stackings of $MX_2$ materials. Atomic force microscopy (AFM) studies of the nanostructure topography have been carried out on over a hundred nanoplates and correlated with LF and high-frequency (HF) Raman spectroscopy of representative plates in a one-to-one fashion. We further explain in a unified structural framework how nanoplates of $WSe_2$ can adopt diverse and complex stacking arrangements, both centrosymmetric and noncentrosymmetric, due to the number and rotation of screw dislocations present and how the nanoplates can exhibit a range of optical and spectroscopic properties including those unexpected and previously not observed. We have classified the diverse nanoplates based on the shape of the dislocation spirals and explained the origin of their layer stackings based on the number and rotation of the screw dislocations and correlated these distinct changes in layer stacking with their physical properties. Even though bulk 3R-$MX_2$[11,29] and noncentrosymmetric $MX_2$[30,38,39] have been observed before, several additional noncentrosymmetric forms of $WSe_2$ with bulk thickness (>6L) and interesting optical properties, namely SHG and photoluminescence (PL), have been observed and characterized for the first time.

## RESULTS AND DISCUSSION

**Synthesis.** Nanoplates of $WSe_2$ were synthesized using CVD onto a native oxide coated silicon substrate using $WO_3$ and Se as precursors (see Materials and Methods and Figure S1 in the SI). Figure 1 shows scanning electron microscope (SEM) and AFM images of the products. A large number of dislocation-driven plates of different shapes, including representative triangular (red circle), hexagonal (blue circle), and mixed shape (green circle), as well as some irregular shapes and occasional flower-like morphologies can be observed (Figure 1a). The size of the plates varies from a few micrometers up to 40 $\mu$m, but the majority are between 10 and 20 $\mu$m. Rapid introduction of Se into the furnace leads to rapid increase in the partial pressure of the Se and gaseous $WO_{3-x}$ precursor species. This sudden increase creates a burst of disordered growth, which results in multiple crystal domains with mismatched crystal lattices. These will serve as the initial dislocation sources and initiate the screw dislocation-driven growth,[36,37] which can be promoted by low supersaturation conditions to produce the dislocated nanoplates.[40] We have successfully grown these plates on native silicon oxide or thick oxide (350 nm) coated Si, fused silica, and sapphire. Additionally, we believe that dislocation growth could be induced intentionally by engineering the substrates to contain dislocations.[41]

Although complete control over the shape and type of the nanoplates grown is difficult to accomplish, some control over the shape of the plates can be achieved: increasing the ratio of the Se:$WO_3$ precursors leads to a larger percentage of hexagons relative to triangles (see Figure S2). The difference in the shape distribution may be a result of the variation of local precursor concentration across the substrate surface, which is a factor that results from using solid precursor materials.[29,31,42] The Se helps to volatilize the $WO_3$ into gaseous $WO_{3-x}$, and thus by

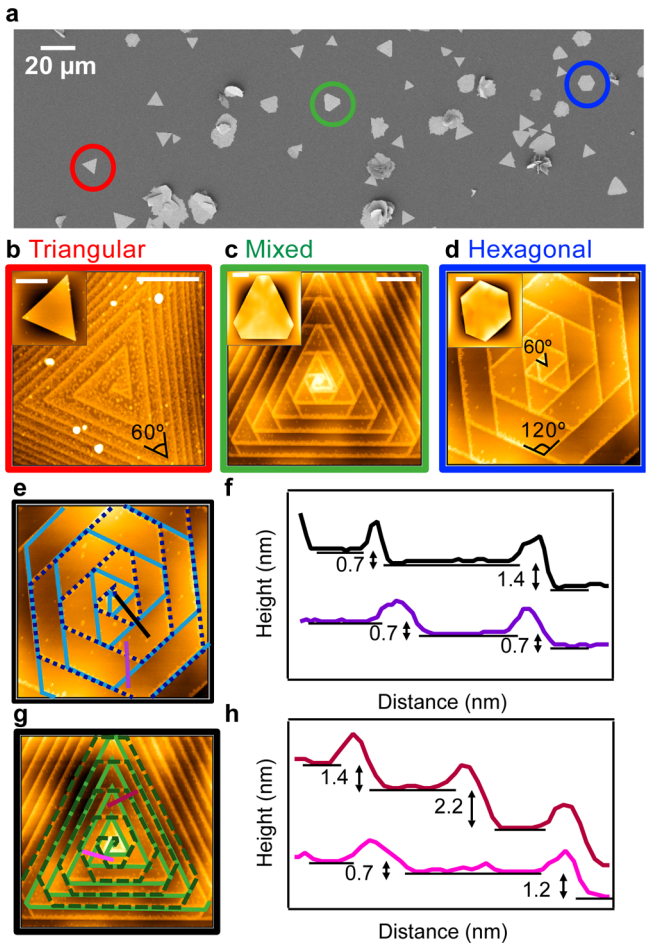


**Figure 1.** (a) Overview SEM image of $WSe_2$ nanoplates grown on a Si substrate. Circles indicate three plates of different shape: triangle (red), hexagon (blue), and mixed (green). (b−d) AFM images of three representative $WSe_2$ nanoplates showing different types of dislocation spiral behaviors, classified as b, triangular, c, mixed, and d, hexagonal. Insets show the overall shape of each plate. Scale bars are 500 nm for the main images and 2 $\mu$m for insets. (e) Trace out of the two dislocation spirals shown in d, one in a solid light blue line and one in a dark blue dotted line, demonstrating that the spirals have a 60° angle between them at the common dislocation core, and are hexagonal away from the core, with 120° angles at the corners. (f) Line profiles along the black and purple lines shown in e. The purple line shows single layer steps (0.7 nm) while the black line shows that there can also be overlap between the two dislocation spirals creating alternating double layer steps (1.4 nm) and single layer steps. (g) Trace out of the two dislocation spirals shown in c, one in a solid light green line and one in a dark green dotted line, showing that one spiral is approximately hexagonal in shape while the other is triangular, creating the mixed designation. (h) Line profiles for the dark and light pink lines shown in g. The dark pink line shows that the triangular dislocation spiral consists of two layers, and where the two dislocations overlap, the step height is three layers. The light pink line shows that the hexagonal spiral step is a single layer, and the triangular spiral step is two layers.



DOI: 10.1021/jacs.6b12559
J. Am. Chem. Soc. 2017, 139, 3496−3504

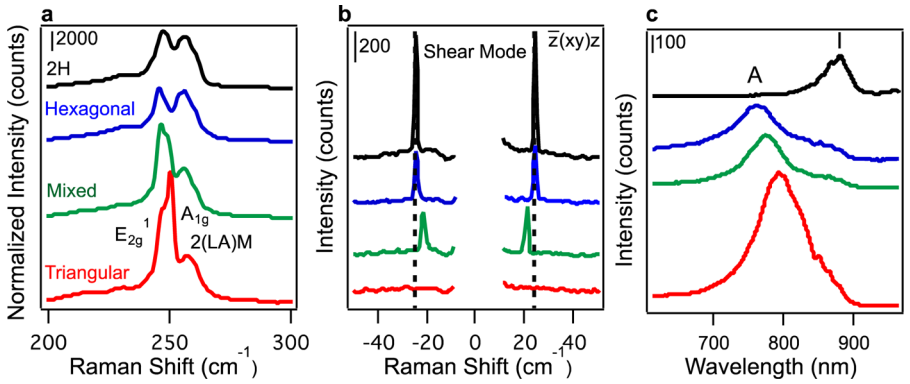


**Figure 2.** (a) High-frequency Raman spectra for a 2H-$WSe_2$ single crystal (black), and $WSe_2$ nanoplates with hexagonal (blue), mixed (green), and triangular (red) spiral dislocations at 532 nm excitation. Intensity has been normalized so that the height of the 2(LA)M peak is the same for all spectra. (b) Low-frequency Raman spectra for the same four samples shown in a, showing both the Stokes and the anti-Stokes regions. Black dotted line is at ±24.7 $cm^{-1}$. (c) Photoluminescence spectra taken on the same four samples as a and b at 532 nm excitation. The A exciton peak and the indirect bandgap peak (I) are labeled. Note that the PL intensity is still much lower for these nanoplates than for a $WSe_2$ monolayer (see Figure S6 in SI).

increasing the amount of Se relative to $WO_3$, a higher partial pressure of both precursors can be achieved.[30] As the edges in a $WSe_2$ hexagon are alternating in W and Se termination, we hypothesize that growth along all six edges is favored when both species are present in sufficient amounts, while growth of only three edges occurs when one species is more dominant than the other, influencing the shape distribution.[42]

**Topography and Classification of Dislocation Spirals.** Beneath the macroscopic shape difference among these nanoplates, we found more profound differences in their micro and nanostructures. AFM studies (Figure 1b–d) reveal that most $WSe_2$ plates contain screw dislocations and display diverse nanoscale surface topography. These screw dislocations vary in number as well as the distinct shapes of the associated spirals, which are correlated with the overall macroscopic shape of each nanoplate, shown in the insets of Figure 1b–d. We categorize the plates based on the dislocation spiral shape that is traced out far (>500 nm) from the dislocation core into three main classes: triangular, hexagonal, and mixed. Figure 1b illustrates a simple example of a plate with a single dislocation spiral that forms a triangular shape, which always has 60° angles at the corners. A more complex example shown in Figure 1d contains two dislocations that share a common core. Dislocation growth spirals due to multiple dislocations have been observed and elucidated for general crystal growth.[43] As illustrated in Figure 1e, tracing out these two dislocation spirals revealed that both have six sides similar to a hexagon, with 120° corners. At the shared dislocation core, the two spirals emerge 60° from each other and wrap in a counterclockwise motion that creates alternating single-layer step edges and bundled double-layer step edges that can be confirmed by AFM height profiles (Figure 1f). The purple line profile in Figure 1f, which follows along the purple line in Figure 1e, shows the step height of a single spiral corresponds to 0.7 nm, or one layer of $WSe_2$. Where the two dislocations overlap, the step height is ∼1.4 nm (Figure 1f, black trace). Note that near the dislocation core, not all sides of the spiral are equally developed, but the angles at each corner are always 120° (for other traced out examples, see Figure S3). Figure 1g shows the two dislocations traced out for the mixed spiral plate shown in Figure 1c, revealing one hexagonally shaped and one triangularly shaped dislocation spiral. Moreover, line profiles (Figure 1h) reveal that the hexagonal spiral is one layer of $WSe_2$ in height, but the triangular spiral is actually 2 layers in height (light pink trace). The dark pink trace shows that where the two dislocations overlap, the step contains three layers. Therefore, mixed plates represent those spirals that are not a symmetric hexagon or triangle, or that contain multiple dislocations that share a common dislocation core and have both hexagonal and triangular spiral shapes. The dislocation hillocks of these plates create a flattened pyramid structure with a steep drop off at the edge of a plate (around 100 nm) and a slight slope up to a maximum height of approximately 150 nm in the center of the plate (see Figure S4). The representative plates shown in Figure 1 all have similar width (4–6 μm) and thickness (90–160 nm), allowing for direct comparison not influenced by their dimensions.

We found that although the overall shapes of the plates generally follow the shapes of the spirals, the macroscopic shape of a plate itself does not necessarily predict the shape of the spiral. As will be further shown below, the types of screw dislocations and the shapes of the spirals are a better predictor of the spectroscopic signature and the layer stacking, and therefore that is how we chose to classify these $WSe_2$ plates. Among the total of 112 plates carefully analyzed with AFM, 62 (55%) contained triangular spirals, 36 (32%) hexagonal spirals, and the remaining 13 (12%) contained mixed or no dislocations. 44% of all triangular spiral plates (27 total) contained a single dislocation (as shown in Figure 1b), while 61% of hexagonal spiral plates (22 total) contained double dislocations, displayed in Figure 1d. Therefore, these two representative examples in Figure 1b and 1d represent a significant fraction (49/112) among all nanoplates; and together with the mixed shape plate shown in Figure 1c, they represent the most common types of plates observed. The remaining plates make up a diverse set of dislocation behaviors that illustrates the high level of complexity observed, summarized by the collection of AFM images in Figure S5 in the SI. Triangular or hexagonal plates with no apparent screw dislocations as well as hexagonal plates with a single hexagonal dislocation spiral are rarely observed (one case each).

**Raman Spectroscopy.** These three classes of nanoplates show very different Raman signatures. Figure 2a shows HF Raman spectra from individual nanostructures with hexagonal (blue line), mixed (green line), and triangular (red line) spiral shapes in comparison with a bulk 2H-$WSe_2$ single crystal (black


DOI: 10.1021/jacs.6b12559
J. Am. Chem. Soc. 2017, 139, 3496–3504

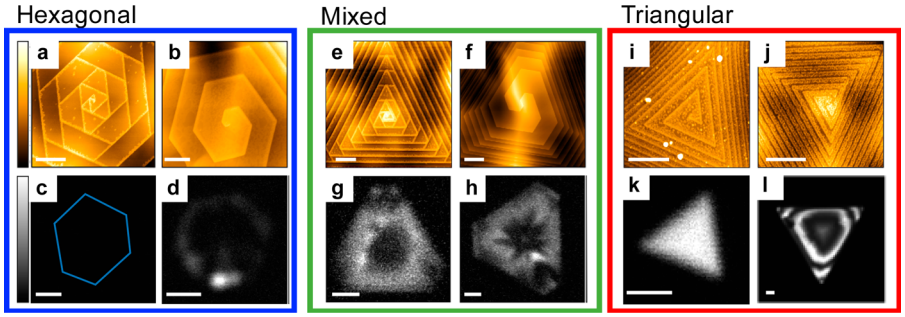


**Figure 3.** AFM and SHG images of representative $WSe_2$ nanoplates in three classes. (a,b) AFM images of the topography of two hexagonal spiral plates with a, two dislocations and b, one dislocation, with the corresponding SHG images of the entire plate (c,d). (e,f) AFM and (g,h) SHG images of two mixed spiral plates each with two dislocations. (i,j) AFM images and (k,l) the corresponding SHG images of two triangular spiral plates with one dislocation (i) and three dislocations (j). Top row scale bars are 500 nm, bottom row scale bars are 2 $\mu$m.

line, "2H"). The plate with hexagonal spirals exhibits a spectrum very similar to that of the 2H-$WSe_2$ single crystal. Both show degenerate $A_{1g}$ and $E^1_{2g}$ peaks at 247 $cm^{-1}$ and a peak at 257 $cm^{-1}$ that is from an overtone of the longitudinal acoustic phonon at the M point in the Brillouin Zone, referred to as a "2(LA)M" phonon peak.[44−46] Plates with triangular spirals, however, have quite different spectra (Figure 2a red trace) in which the $A_{1g}$ peak at around 251 $cm^{-1}$ is now clearly distinguishable from the neighboring $E^1_{2g}$ peak at 247 $cm^{-1}$, indicating a break in the degeneracy of the out-of-plane and in-plane vibrations, respectively. Both peaks, especially the $A_{1g}$ peak, have also been enhanced relative to the 257 $cm^{-1}$ 2(LA)M phonon peak. Raman spectra of this nature has been observed before, but typically only for few-layer $WSe_2$.[44,45] For mixed spiral plates, the spectrum (Figure 2a green trace) shows a similar $E^1_{2g}$ peak enhancement but now the $A_{1g}$ peak has been partially suppressed relative to the triangular spiral plate spectrum. These changes in the $A_{1g}$ and $E^1_{2g}$ Raman peaks indicate that there are differences in the interlayer interactions that affect the vibrational modes, which suggests a change in the layer stacking among different types of $WSe_2$ nanoplates.

LF Raman is an effective method for determining the crystal phase of $MX_2$ materials, as the interlayer breathing and shear modes of these materials are very sensitive to layer stacking.[14,47] Figure 2b shows LF Raman spectra collected in the $\bar{z}(x,y)z$ polarization configuration, using the Porto notation[48] (see Materials and Methods). Bulk 2H-$WSe_2$ is predicted to have one strong shear peak at 24.8 $cm^{-1}$.[49] The $WSe_2$ plates with hexagonal spirals exhibit a Raman feature at 24.7 $cm^{-1}$, nearly identical to that of the 2H single crystal, while the mixed spiral plates show a sharp peak shifted to lower frequency (21.5 $cm^{-1}$) and the triangular spiral plates show no detectable LF Raman features. As expected, no breathing modes were observed for our samples under the $\bar{z}(x,x)z$ polarization configuration because these modes are forbidden in bulk form.[49] The absence of a LF Raman peak for the triangular spiral plates indicates significantly reduced interlayer interactions, thereby leading to Raman shifts below the smallest value we can measure (~10 $cm^{-1}$). This means the layer stacking in the triangular plates is quite different from that commonly seen for $WSe_2$.

For mixed spiral plates (Figure 2b green curve), the shift to lower frequency suggests that these samples have reduced interlayer interactions compared to 2H that may arise from a stacking arrangement in-between that of the hexagonal and triangular plates. We have also compared the ratio of intensities of the LF shear peak to the HF $E^1_{2g}$ peak for each type to show their very different stacking arrangements (see SI for more discussion). Both HF and LF Raman data clearly show that many of the dislocated $WSe_2$ plates exhibit different interlayer interactions and stacking arrangements from the bulk 2H-$WSe_2$ materials.

**Photoluminescence.** Photoluminescence (PL) data reveal that these dislocated $WSe_2$ plates also have different optical properties (Figure 2c), although the PL intensity observed is still much weaker than that of monolayer $WSe_2$ (see Figure S6 for a comparison). Hexagonal spiral plates display a PL peak with a small intensity attributable to the A exciton peak around 765 nm (labeled A). This is slightly shifted from literature values for a $WSe_2$ monolayer, which typically displays the peak between 750[9] and 760 nm.[50] This result is in direct contrast with single-crystal 2H-$WSe_2$ for which the only observable PL is derived from the indirect bandgap transition at 850 nm (labeled I).[50] The small PL intensity from the A exciton peak of the nanoplates could be due to defects within the $MX_2$ plates that are allowing for a relaxation followed by radiative recombination that can lead to enhanced PL intensity.[51,52] Evidence of this relaxation to a defect state can be observed when comparing the PL data to optical absorbance data (Figure S7), as the A exciton peak in the PL spectra is red-shifted from that in the absorbance spectra.[53] Further work is required to fully understand the source of the PL in the hexagonal nanoplates.

Interestingly, as the dislocation spiral changes from hexagonal to mixed to triangular shape, there is a red shift of this A exciton peak from 765 to 775 to 795 nm, which is similar to values between 770[54] and 785 nm[55] that have been observed for multilayer $WSe_2$ resulting from reduced energy of the direct bandgap transition. Additionally, the PL intensity for triangular spiral plates is 2.5 times greater than for hexagonal spiral plates. Furthermore, the absorbance spectra and X-ray diffraction (XRD) (Figure S8) demonstrate different interlayer coupling and decreased layer spacing, which are consistent with the changes in the PL intensity and peak position of the individual nanoplates. The absorbance spectra reveal that the splitting between the A and B excitonic peaks is 0.55 eV for the hexagonal plates and 0.48 eV for the triangular nanoplates. The reduced peak splitting for the triangular plates suggests less interlayer coupling than for the hexagonal plates. A reduction in interlayer coupling has been shown to promote PL,[22] effectively explaining why the triangular nanoplates have higher PL than the hexagonal nanoplates.

**Second-Harmonic Generation Imaging.** SHG imaging was conducted to further probe the symmetry and layer


DOI: 10.1021/jacs.6b12559
J. Am. Chem. Soc. 2017, 139, 3496−3504

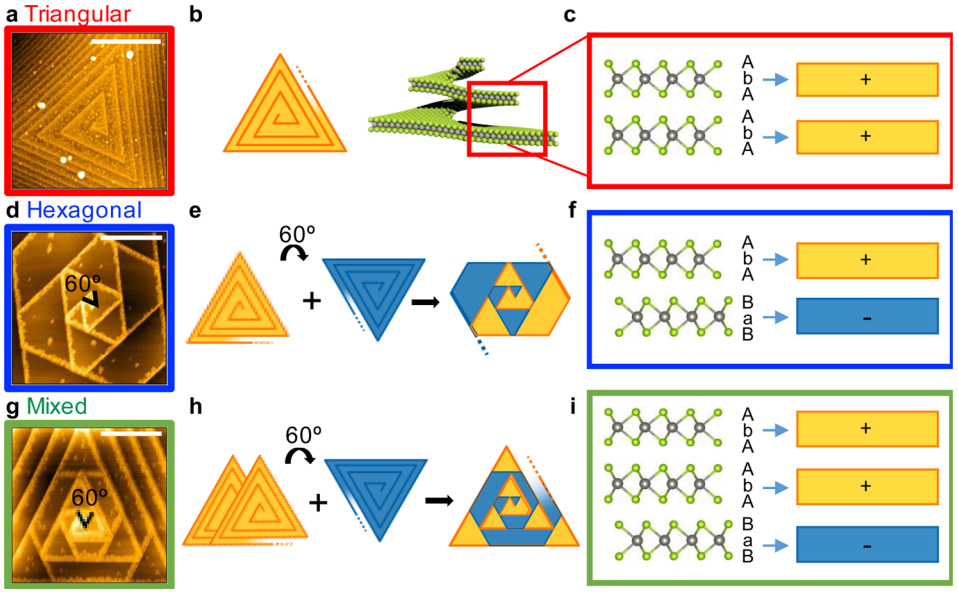


**Figure 4.** Layer stacking schemes for various dislocated $WSe_2$ nanoplates. (a) AFM image of a triangular spiral plate with a single dislocation, represented in a top down schematic view and a 3D perspective view in (b). The gray atoms are W and the light green are Se. (c) Side view of two layers of the triangle, displaying AbA AbA stacking, which can be denoted simply as + + stacking. (d) AFM image of a hexagonal spiral plate with two dislocation spirals rotated 60° from each other. This image is a magnified image of the plate shown in Figure 1d. (e) A top down schematic view of a dislocation spiral (yellow) plus a second dislocation spiral with a 60° rotation (blue) to create the double dislocation spiral. (f) A side view of the atoms demonstrates that the second dislocation is now a different orientation from the first, creating AbA BaB stacking, which is denoted simply as the + − stacking. (g) AFM image of a mixed spiral plate with two dislocations, a magnified view of the plate shown in Figure 1c. (h) Top down schematic view of two dislocation spirals stacked on top of each other plus a third dislocation spiral at a 60° rotation which combine to create the three-dislocation spiral pattern shown. (i) Side view of the three-layer stacking that results from the dislocation arrangement in h, creating a + + − layer stacking. Scale bars for a, d, and g are 500 nm.

stacking of the $WSe_2$ plates. Theoretically, only noncentrosymmetric crystal structures generate SHG signal. Note that this noncentrosymmetry refers to the lack of inversion center across the layered crystal structures, not the macroscopic shape they might adopt (i.e., triangles vs hexagons). On the basis of this criterion, there should be no SHG signal for the centrosymmetric bulk 2H-$WSe_2$. Indeed, a control measurement completed on a $WSe_2$ single crystal did not show any measurable SHG. Figure 3 compares examples of the three primary classes of $WSe_2$ nanoplates, showing SHG images of the entire plate (bottom row) together with the corresponding AFM images of the center of the plate (top row). Plates containing both one (Figure 3b) and two (Figure 3a) hexagonal dislocation spirals do not exhibit any SHG intensity except at defects and edges (Figure 3c and d), indicating that the hexagonal nanoplates are centrosymmetric. Interestingly, strong SHG signal was observed for the nanoplates with triangular dislocation spirals, suggesting a noncentrosymmetric crystal structure (Figure 3i–l). For larger plates containing single or multiple dislocations with triangular spirals, variations in the intensity of the SHG signal across the surface of the plate start to emerge, resulting in rings (Figure 3l) as well as other patterns (Figure S5). We attribute these patterns to interference of the SHG signal because they only start to develop when the plates become large enough for the laser wavelength to modulate the ring pattern periodicity (see Figure S9 and S10). Figure 3e–h show that plates with mixed spiral shapes exhibit SHG as well, although the intensity is not as strong as that of the triangular spiral plates. The relative intensities of the different types of plates are compared directly in the same field of view in Figure S11 in the SI to show that the variation in SHG intensity is substantial across the three types of plates. The HF and LF Raman spectra (Figure S12) for the specific plates shown in Figure 3 confirm that they follow the same trends described in Figure 2.

**Creating Different Layer Stackings Using (Multiple) Screw Dislocations.** The Raman, PL, and SHG results observed above clearly reveal that there are layer stacking changes among different classes of dislocated nanoplates. But how do screw dislocations create these different centrosymmetric or noncentrosymmetric layer stacking sequences in $MX_2$ materials? Figure 4 illustrates our proposed model for explaining the formation of the diverse stacking sequence using single or multiple screw dislocations in a unified structural framework. Typically, the layer stacking of a 2H-$MX_2$ structure is represented as AbA BaB, and for 3R it is AbA CaC BcB,[56] where the capital letters denote the positions of the X atoms and the lowercase letters denote the positions of the M atoms, and each triplet of AbA or BaB denotes a single $MX_2$ layer. The key difference between 2H and 3R is that the 3R stacking consists of just a translation of the $MX_2$ layers from each other, while the 2H involves a rotation of one $MX_2$ layer by 60 or 180° from the other (see SI Figure S13 for details). This rotation leads to the formation of the BaB layer that is not present in the 3R phase and a switch from noncentrosymmetry to centrosymmetry, creating a dramatic change in properties and layer interactions. For the dislocated plates, we will use these basic ideas to determine and illustrate the layer stacking, but ignore the details about translation of the layers.

For the most straightforward case of the single dislocation triangle (Figure 4a), the presence of a screw dislocation creates a shear (line break) within one layer, such that the $MX_2$ layer continuously spirals and stacks directly on top of itself, so each subsequent layer (in fact, all of them are one continuous spiral


DOI: 10.1021/jacs.6b12559
J. Am. Chem. Soc. 2017, 139, 3496–3504

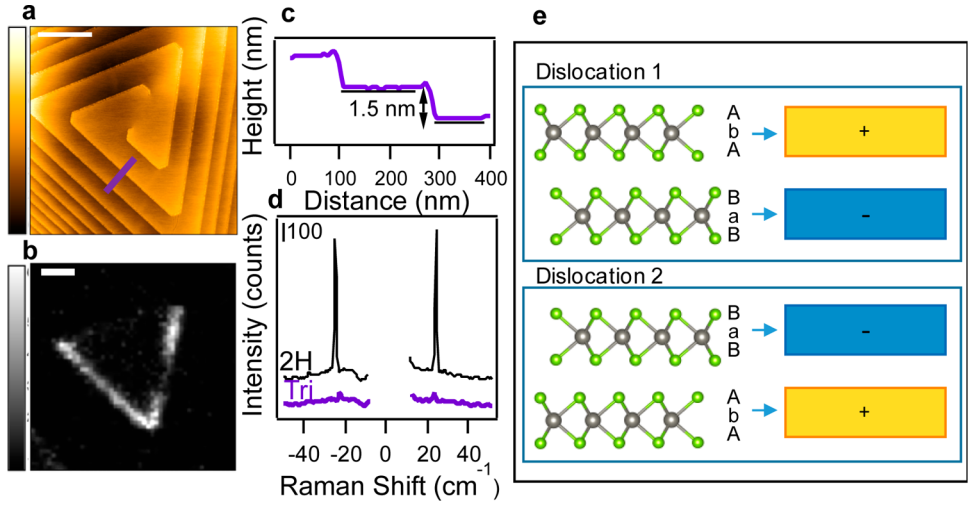


**Figure 5.** (a) AFM image of a $WSe_2$ plate that contains two dislocation cores separated from each other, each with a dislocation that traces out a triangular spiral shape. Scale bar 500 nm. (b) Corresponding SHG image of the entire plate showing no intensity in the center of the plate. Scale bar 2 $\mu$m. (c) AFM line profile along the purple line in a that shows that each step contains two layers of $WSe_2$. (d) Low-frequency Raman spectra of 2H-$WSe_2$ single crystal (black) and the plate shown in a, labeled tri for triangular spiral shape (purple). (e) Schematic illustration of the proposed layer stacking for the plate shown in a, which consists of a + − bilayer and a − + bilayer, creating a pseudo-2H phase.

layer) is effectively at 0° rotation, as shown in a top down and 3D perspective view in Figure 4b. No rotation of the layer is possible, therefore, as shown in Figure 4c, the layer stacking becomes AbA AbA. We can further simplify the notation to "+ +", which only represents the asymmetric direction of the $MX_2$ layers. The + + notation here is similar to the AA[30] and 3R[14] stacking notations invoked in the literature, except that it ignores the translation of the layers and detailed atomic positions. A + + stacking arrangement would not have inversion symmetry and hence would have strong SHG (see Figure 3k) and weak interlayer interactions, as demonstrated by the LF Raman in Figure 2b (red trace). This stacking assignment also agrees with one recent report that predicted a hypothetical 3R bulk phase of $WSe_2$ (which would have a "+ + +" notation) would not exhibit a shear peak in the LF Raman due to less atomic displacement of the layers in this stacking arrangement.[17] Indeed, for few-layer $WSe_2$, the 3R phase is calculated to be slightly less stable, and shown to have a downshift in the frequency as well as a decrease in the intensity of the shear peak.[14]

Now, in order to obtain inversion symmetry, one $MX_2$ layer must be rotated relative to the other by either 60° or 180°. The hexagonal spiral plate shown in Figure 4d contains one single layer dislocation spiral similar to that shown in Figure 4b and another single layer dislocation spiral that emerges with a 60° angle from the first one (Figure 4e), which thus creates a change from a + + layer stacking to a + − layer stacking with inversion symmetry (Figure 4f). The − sign here indicates that the $MX_2$ layer has been rotated relative to the first layer, similar to the 2H stacking of AbA BaB. The inversion symmetry is determined by the rotation of the layers, not by the translation, and therefore although there could be small changes in the translation of the $MX_2$ layers, it will not change the overall centrosymmetry that these nanoplates contain. The repeating + − layer stacking will create strong interlayer interactions, no SHG, and a sharp shear peak in the LF Raman, all of which have been observed for the hexagonal spiral nanoplates.

For the more complex mixed shape plate shown in Figure 4g, the layer stacking is a result of both the rotation of the layers and the number of layers in each dislocation spiral. Recall that this plate contains two dislocations rotated by 60° from each other, but the triangular dislocation spiral contains two layers (shown in Figure 1g, h). This extra layer, shown in Figure 4h, will not have a different orientation from the layer it spirals with. But the third dislocation spiral layer rotated by 60° must be the opposite orientation from the double-layer dislocation, and therefore the resulting layer stacking would be + + − (Figure 4i). The LF Raman would be shifted and reduced in intensity compared to the standard + − stacking, as now the interactions between the layers are not uniform throughout. Such + + − layer stacking is still noncentrosymmetric over the whole structure but local inversion symmetry between + − layers exists; therefore, it would have reduced SHG intensity compared to the + + stacking, as shown above in Figure 3. The multiple layer dislocation spirals with no rotations or rotations of 120° lead to essentially the same overall + + stacking, even though the grouping into each dislocation spiral can vary; this leads to strong SHG signal for all triangular spiral plates observed with multiple dislocations sharing a single core. The proposed layer stacking arrangements (depicted using the + and − notation) for the remaining plates shown in Figure 3 as well as other examples are illustrated in Figure S5. These dislocated nanoplates can be satisfactorily explained based on the combination of the number and rotation of elementary triangular dislocation spirals.

**Nanoplates with Increased Complexity.** After the relatively simple prototypes have been understood, we can explain the increased complexity that is introduced based on the number, rotation, and further, the locations of the screw dislocations. We first compare two $WSe_2$ plates with triangular spirals, one that contains a single dislocation (Figure 3i) and another with two dislocations at two distinct cores (Figure 5a). As discussed above, the former has + + stacking and very strong SHG signal (Figure 3k), while the latter has completely quenched signal in the center of the plate (Figure 5b). This observation is unlike the observed interference patterns (Figure 3l) that still display weak SHG intensity in the center due to incomplete interference, suggesting that the lack of SHG signal


DOI: 10.1021/jacs.6b12559
J. Am. Chem. Soc. 2017, 139, 3496−3504

is due to the return of centrosymmetry to the crystal structure. HF Raman spectrum for this plate shows the enhanced $A_{1g}$ peak at 251 $cm^{-1}$ typically seen for triangular dislocation spirals (see Figure S14). In contrast to the single core triangular dislocation spiral that displays no LF Raman peaks (Figure 2b), the plate with two triangular spiral dislocations with offset cores displays a small peak around 23 $cm^{-1}$ (Figure 5d purple trace), indicating a layer stacking that is closer to that of the hexagonal spiral plates with + − stacking. Upon closer examination, an AFM line profile (Figure 5c) shows that each dislocation spiral step contains two layers of $WSe_2$ (height ∼1.5 nm). We hypothesize that the two dislocation cores initiate two sets of two layers spiraling around each other in a pseudo-2H phase, creating properties that are similar to the standard 2H phase. We believe that these two dislocations originate from the same set of layers initially but on opposite sides of each other. If originally there were three layers that were + − + stacked, one dislocation could have emerged on the first two + − layers while the other could have emerged for the top two − + layers (both dislocations share the middle − layer). The result would be a stacking of + − − +, illustrated in Figure 5e where the layer stacking is modeled as pairs of layers. Essentially this creates an AB repeating unit, except that now the "A" and "B" each contain two layers of opposite orientation. This unique paired stacking creates a pseudo-2H stacking behavior that restores centrosymmetry in regions far from the edge of the plate. The small amount of SHG at the edges could be due to the fact that one of the spirals does not wind all the way to the edge, creating some defects. Even more complex plates can be formed when dislocations coexist with layer-by-layer growth regions to create changes in layer stacking within a single nanoplate (see Figure S15 and additional discussion in SI).

We have shown that the layer stackings in dislocated $WSe_2$ nanoplates can deviate from the simple 2H to complex and noncentrosymmetric stackings due to the variations of the rotation and number of the screw dislocations present in the plates. Figure S5 in the SI further shows the sheer number of diverse dislocation varieties and the corresponding SHG images, as well as the proposed +/− layer stacking arrangement for each nanoplate. Every nanoplate example shown herein is unique in the number, location, and rotation arrangements of dislocations, and it is likely that this collection is not exhaustive. The corresponding layer stacking arrangements, when represented in the simplest + − notation (i.e., neglecting the details of layer translations) and observed as a whole (i.e., ignoring which dislocation each layer is associated with), are more limited. Extensive results presented herein, using a suite of microscopy and spectroscopy techniques, clearly show that screw dislocations play a more fundamental and differential role in determining the layer stacking patterns and thus the resulting optical properties than the apparent macroscopic shape (see images in Figure S5 with pink boxes). The layer stacking that results from the number and rotation of the dislocations involved appears to determine the morphology of the spiral shape (though the full details regarding the growth mechanism under different growth conditions remain to be understood), hence the classification of the dislocation spiral shapes is a convenient way to identify the layer stacking of these plates. Essentially, all triangular spiral plates with a single core have the most noncentrosymmetric + + stacking that is similar (but not identical) to the 3R (ABC) stacking, and all hexagonal spiral plates have the centrosymmetric + − stacking that is similar to 2H, and all mixed and complex plates have some version of intermediate stacking, such as + + −, + + + −, or + − − +. Moreover, in the perspective of bulk solid state compounds, these complex stacking sequences of $WSe_2$ should also be viewed as new structural polymorphs of the simple 2H-$WSe_2$ structure, which might be compared to the well-known example of SiC which displays many structural polymorphs.[57] Notably, a variety of noncentrosymmetric layer stackings of many-layer $WSe_2$ structures directly grown by CVD has, to the best of our knowledge, not yet been elucidated, and this lack of centrosymmetry is important for SHG[23] and valleytronics.[2,11]

## ■ CONCLUSION

Our results demonstrate that screw dislocations can change the layer stackings of $WSe_2$ nanoplates, providing access to a variety of complex and unconventional stacking arrangements with new and interesting properties that have not been observed in bulk or previous few-layer materials. Furthermore, we have clearly explained how the stacking is determined by the rotation and number of the elementary triangular dislocation spirals, which relates to the symmetry of the dislocation spirals and can be categorized in three classes: triangular, hexagonal, and mixed. Triangular spiral plates adopt a noncentrosymmetric phase (AA stacking) with strong SHG signal and enhanced PL, while hexagonal spiral plates adopt the simple centrosymmetric 2H (AB) stacking. Mixed spiral plates fall between these two categories, creating a variety of weakly noncentrosymmetric layer stacking arrangements with varying properties previously not observed for $WSe_2$ materials. The understanding developed here should be generalizable to other layered materials in that under appropriate conditions, any $MX_2$ materials containing screw dislocations could also form such complex layer stacking arrangements, realizing diverse properties within the *same* material composition. Although evidence of the triangular AA stacked dislocation spirals has been observed previously,[30] the range of layer stackings and properties achievable with screw dislocations has not been demonstrated thus far, and the understanding presented here can open up the study of these materials for a broad array of applications, such as optoelectronics, spintronics, and valleytronics.

## ■ MATERIALS AND METHODS

**Synthesis of $WSe_2$ Nanoplates.** $WSe_2$ nanoplates were grown on both (111) and (100) silicon substrates covered with native silicon oxide via a chemical vapor deposition process using $WO_3$ and Se as precursors. The silicon substrates were sonicated in IPA, acetone, ethanol, and nanopure water and dried with $N_2$ gas prior to the reaction. $WO_3$ powder (approximately 300 mg) was placed in an alumina boat in the center of a Lindberg Blue M tube furnace, and the silicon substrates were placed face down on top of the boat. Another boat filled with Se powder (approximately 600 mg) was placed outside the heating zone of the tube furnace. The CVD system was preheated at 200 °C for 10 min under an argon flow rate of 120 sccm to drive off the moisture in the system. The tube was then heated to 880 °C under a pressure of 780 Torr with an argon flow of 50 sccm. Once at the reaction temperature, the Se boat was pushed into the heating zone of the tube furnace by using magnets so that the front of the boat was at a temperature of 600 °C. Simultaneously, $H_2$ gas was turned on at a flow rate of 2 sccm. At 2 and 4 min, the Se boat was pushed slightly farther into the tube furnace and finally at 5 min the Se boat was pushed completely inside the furnace. The reaction went on for 7−10 min before the furnace was cooled down naturally.

**Characterization of $WSe_2$ Nanoplates.** The nanoplates were routinely characterized using an optical microscope (Olympus BX51M), scanning electron microscope (LEO SUPRA 55 VP field-emission SEM) operated at 3 kV, atomic force microscope (Agilent


DOI: 10.1021/jacs.6b12559
J. Am. Chem. Soc. 2017, 139, 3496−3504

5500), and high-frequency Raman spectrometer (LabRAM Aramis Confocal Raman/PL Microscope). The high-frequency Raman measurements were completed using a 532 nm laser and a 100× microscope objective.

**Second-Harmonic Generation Imaging.** Second-harmonic generation imaging was completed at the Laboratory for Optical and Computational Instrumentation at UW−Madison using a Prairie Ultima microscope system equipped with a Spectra Physics Insight laser at an excitation wavelength of 890 nm and a 100× microscope objective (N/A = 0.8). Backward direction SHG signal was filtered using a 445/30 bandpass filter (Semrock) to ensure only light around 445 nm, the expected SHG signal response, was observed.

**Photoluminescence Measurements.** PL measurements were carried out at the Center for Nanoscale Materials at Argonne National Lab using a home-built setup. A Fianium Supercontinuum Fiber Laser was used and 532 nm light was selected using an Acousto-Optic Tunable Fiber (AOTF), with an average power of 200 $\mu$W. The light was focused onto the sample using an Olympus IX-71 inverted microscope and a 100× objective (N/A = 0.9). The PL was collected and analyzed using a spectrometer (Princeton Instruments SP2360) equipped with a CCD camera (Princeton Instruments PIXIS 100BR).

**Low-Frequency Raman Measurements.** Low-frequency Raman experiments were carried out at the Center for Nanophase Materials Sciences at Oak Ridge National Lab using a Jobin-Yvon T64000 triple spectrometer with a liquid nitrogen cooled CCD detector. A 532 nm laser light was used and focused onto the sample with a 100× objective (N/A = 0.9) and a spot size of about 1 $\mu$m, at an excitation laser power of 640 $\mu$W. Polarized Raman measurements were carried out by inserting a polarizer and a half-wave plate into the scattered beam path to get the $\bar{z}(x,y)z$ polarization configuration, using the Porto notation[14,48] where $\bar{z}$ and $z$ represent the propagation direction and $x$ and $y$ represent the polarization direction of the incident and scattered light, respectively. The polarization configuration had reduced Rayleigh scattering effects from the plates compared to the $\bar{z}(x,x)z$ configuration.

## ■ ASSOCIATED CONTENT

### Supporting Information

The Supporting Information is available free of charge on the ACS Publications website at DOI: 10.1021/jacs.6b12559.

Schematic of the CVD growth of $WSe_2$ nanoplates, additional SEM and AFM images of the different types of plates, corresponding SHG images and layer stacking illustrations for these plates, additional PL and Raman data, absorbance and XRD data, a comparison of the 2H and the 3R stacking arrangements, and an example of a single plate that contains multiple layer stackings (PDF)

## ■ AUTHOR INFORMATION


### Corresponding Authors

*rjhamers@chem.wisc.edu

*jin@chem.wisc.edu

### ORCID

Melinda J. Shearer: 0000-0001-6121-3614

Robert J. Hamers: 0000-0003-3821-9625

Song Jin: 0000-0001-8693-7010


### Notes

The authors declare no competing financial interest.

## ■ ACKNOWLEDGMENTS

This research is supported by the Department of Energy, Office of Basic Energy Sciences, Division of Materials Science and Engineering, under Award DE-FG02-09ER46664. M.J.S. and L.S. also thank the National Science Foundation Graduate Research Fellowship Program under Grant No. DGE-1256259 for support. Support was also provided by the Graduate School and the Office of the Vice Chancellor for Research and Graduate Education at the University of Wisconsin−Madison with funding from the Wisconsin Alumni Research Foundation. The authors also thank Professor Bruce Parkinson for supplying the 2H-$WSe_2$ single crystal. The low-frequency Raman spectroscopy was conducted at the Center for Nanophase Materials Sciences, which is a DOE Office of Science User Facility. M.J.S. would like to thank Dr. David Gosztola for helping with the photoluminescence and absorbance measurements performed at the Center for Nanoscale Materials at Argonne National Laboratory, which is supported by the U.S Department of Energy, Office of Basic Energy Sciences, under Contract No. DE-AC02-06CH11357. M.J.S. and L.S. would like to thank Dr. Josh Weber for his help conducting the second-harmonic generation measurements, performed at the Laboratory for Optical and Computational Instrumentation at UW−Madison.

## ■ REFERENCES


(1) Mak, K. F.; Shan, J. *Nat. Photonics* **2016**, *10*, 216.

(2) Xiao, D.; Liu, G.-B.; Feng, W.; Xu, X.; Yao, W. *Phys. Rev. Lett.* **2012**, *108*, 196802.

(3) Han, W. *APL Mater.* **2016**, *4*, 032401.

(4) Zeng, H.; Dai, J.; Yao, W.; Xiao, D.; Cui, X. *Nat. Nanotechnol.* **2012**, *7*, 490.

(5) Schaibley, J. R.; Yu, H.; Clark, G.; Rivera, P.; Ross, J. S.; Seyler, K. L.; Yao, W.; Xu, X. *Nature Reviews Materials* **2016**, *1*, 16055.

(6) Lukowski, M. A.; Daniel, A. S.; Meng, F.; Forticaux, A.; Li, L.; Jin, S. *J. Am. Chem. Soc.* **2013**, *135*, 10274.

(7) Deng, D.; Novoselov, K. S.; Fu, Q.; Zheng, N.; Tian, Z.; Bao, X. *Nat. Nanotechnol.* **2016**, *11*, 218.

(8) Mak, K. F.; Lee, C.; Hone, J.; Shan, J.; Heinz, T. F. *Phys. Rev. Lett.* **2010**, *105*, 136805.

(9) Zhao, W. J.; Ghorannevis, Z.; Chu, L. Q.; Toh, M. L.; Kloc, C.; Tan, P. H.; Eda, G. *ACS Nano* **2013**, *7*, 791.

(10) Shen, T.; Penumatcha, A. V.; Appenzeller, J. *ACS Nano* **2016**, *10*, 4712.

(11) Suzuki, R.; Sakano, M.; Zhang, Y. J.; Akashi, R.; Morikawa, D.; Harasawa, A.; Yaji, K.; Kuroda, K.; Miyamoto, K.; Okuda, T.; Ishizaka, K.; Arita, R.; Iwasa, Y. *Nat. Nanotechnol.* **2014**, *9*, 611.

(12) Voiry, D.; Yamaguchi, H.; Li, J.; Silva, R.; Alves, D. C. B.; Fujita, T.; Chen, M.; Asefa, T.; Shenoy, V. B.; Eda, G.; Chhowalla, M. *Nat. Mater.* **2013**, *12*, 850.

(13) Kappera, R.; Voiry, D.; Yalcin, S. E.; Branch, B.; Gupta, G.; Mohite, A. D.; Chhowalla, M. *Nat. Mater.* **2014**, *13*, 1128.

(14) Puretzky, A. A.; Liang, L. B.; Li, X. F.; Xiao, K.; Wang, K.; Mahjouri-Samani, M.; Basile, L.; Idrobo, J. C.; Sumpter, B. G.; Meunier, V.; Geohegan, D. B. *ACS Nano* **2015**, *9*, 6333.

(15) Voiry, D.; Mohite, A.; Chhowalla, M. *Chem. Soc. Rev.* **2015**, *44*, 2702.

(16) Ding, Q.; Meng, F.; English, C. R.; Caban-Acevedo, M.; Shearer, M. J.; Liang, D.; Daniel, A. S.; Hamers, R. J.; Jin, S. *J. Am. Chem. Soc.* **2014**, *136*, 8504.

(17) Luo, X.; Lu, X.; Cong, C.; Yu, T.; Xiong, Q.; Ying Quek, S. *Sci. Rep.* **2015**, *5*, 14565.

(18) Geim, A. K.; Grigorieva, I. V. *Nature* **2013**, *499*, 419.

(19) Liu, K.; Zhang, L.; Cao, T.; Jin, C.; Qiu, D.; Zhou, Q.; Zettl, A.; Yang, P.; Louie, S. G.; Wang, F. *Nat. Commun.* **2014**, *5*, 4966.

(20) van der Zande, A. M.; Kunstmann, J.; Chernikov, A.; Chenet, D. A.; You, Y.; Zhang, X.; Huang, P. Y.; Berkelbach, T. C.; Wang, L.; Zhang, F.; Hybertsen, M. S.; Muller, D. A.; Reichman, D. R.; Heinz, T. F.; Hone, J. C. *Nano Lett.* **2014**, *14*, 3869.

(21) Puretzky, A. A.; Liang, L.; Li, X.; Xiao, K.; Sumpter, B. G.; Meunier, V.; Geohegan, D. B. *ACS Nano* **2016**, *10*, 2736.

(22) Huang, S.; Ling, X.; Liang, L.; Kong, J.; Terrones, H.; Meunier, V.; Dresselhaus, M. S. *Nano Lett.* **2014**, *14*, 5500.




DOI: 10.1021/jacs.6b12559
J. Am. Chem. Soc. 2017, 139, 3496−3504

(23) Hsu, W.-T.; Zhao, Z.-A.; Li, L.-J.; Chen, C.-H.; Chiu, M.-H.; Chang, P.-S.; Chou, Y.-C.; Chang, W.-H. *ACS Nano* **2014**, *8*, 2951.
(24) Huang, S.; Liang, L.; Ling, X.; Puretzky, A. A.; Geohegan, D. B.; Sumpter, B. G.; Kong, J.; Meunier, V.; Dresselhaus, M. S. *Nano Lett.* **2016**, *16*, 1435.
(25) Yu, W. J.; Liu, Y.; Zhou, H.; Yin, A.; Li, Z.; Huang, Y.; Duan, X. *Nat. Nanotechnol.* **2013**, *8*, 952.
(26) Gong, Y.; Lin, J.; Wang, X.; Shi, G.; Lei, S.; Lin, Z.; Zou, X.; Ye, G.; Vajtai, R.; Yakobson, B. I.; Terrones, H.; Terrones, M.; Tay; Beng, K.; Lou, J.; Pantelides, S. T.; Liu, Z.; Zhou, W.; Ajayan, P. M. *Nat. Mater.* **2014**, *13*, 1135.
(27) Duan, X.; Wang, C.; Shaw, J. C.; Cheng, R.; Chen, Y.; Li, H.; Wu, X.; Tang, Y.; Zhang, Q.; Pan, A.; Jiang, J.; Yu, R.; Huang, Y.; Duan, X. *Nat. Nanotechnol.* **2014**, *9*, 1024.
(28) Samad, L.; Bladow, S. M.; Ding, Q.; Zhuo, J.; Jacobberger, R. M.; Arnold, M. S.; Jin, S. *ACS Nano* **2016**, *10*, 7039.
(29) Chen, L.; Liu, B. L.; Abbas, A. N.; Ma, Y. Q.; Fang, X.; Liu, Y. H.; Zhou, C. W. *ACS Nano* **2014**, *8*, 11543.
(30) Zhang, L. M.; Liu, K. H.; Wong, A. B.; Kim, J.; Hong, X. P.; Liu, C.; Cao, T.; Louie, S. G.; Wang, F.; Yang, P. D. *Nano Lett.* **2014**, *14*, 6418.
(31) Sarma, P. V.; Patil, P. D.; Barman, P. K.; Kini, R. N.; Shaijumon, M. M. *RSC Adv.* **2016**, *6*, 376.
(32) Ly, T. H.; Zhao, J.; Kim, H.; Han, G. H.; Nam, H.; Lee, Y. H. *Adv. Mater.* **2016**, *28*, 7723.
(33) Zhuang, A.; Li, J.-J.; Wang, Y.-C.; Wen, X.; Lin, Y.; Xiang, B.; Wang, X.; Zeng, J. *Angew. Chem.* **2014**, *126*, 6543.
(34) Forticaux, A.; Dang, L. N.; Liang, H. F.; Jin, S. *Nano Lett.* **2015**, *15*, 3403.
(35) Morin, S. A.; Forticaux, A.; Bierman, M. J.; Jin, S. *Nano Lett.* **2011**, *11*, 4449.
(36) Morin, S. A.; Bierman, M. J.; Tong, J.; Jin, S. *Science* **2010**, *328*, 476.
(37) Bierman, M. J.; Lau, Y. K. A.; Kvit, A. V.; Schmitt, A. L.; Jin, S. *Science* **2008**, *320*, 1060.
(38) Ribeiro-Soares, J.; Janisch, C.; Liu, Z.; Elías, A. L.; Dresselhaus, M. S.; Terrones, M.; Cançado, L. G.; Jorio, A. *2D Mater.* **2015**, *2*, 045015.
(39) Wang, G.; Marie, X.; Gerber, I.; Amand, T.; Lagarde, D.; Bouet, L.; Vidal, M.; Balocchi, A.; Urbaszek, B. *Phys. Rev. Lett.* **2015**, *114*, 097403.
(40) Meng, F.; Morin, S. A.; Forticaux, A.; Jin, S. *Acc. Chem. Res.* **2013**, *46*, 1616.
(41) Morin, S. A.; Jin, S. *Nano Lett.* **2010**, *10*, 3459.
(42) Wang, S.; Rong, Y.; Fan, Y.; Pacios, M.; Bhaskaran, H.; He, K.; Warner, J. H. *Chem. Mater.* **2014**, *26*, 6371.
(43) Shtukenberg, A. G.; Zhu, Z.; An, Z.; Bhandari, M.; Song, P.; Kahr, B.; Ward, M. D. *Proc. Natl. Acad. Sci. U. S. A.* **2013**, *110*, 17195.
(44) Luo, X.; Zhao, Y. Y.; Zhang, J.; Toh, M. L.; Kloc, C.; Xiong, Q. H.; Quek, S. Y. *Phys. Rev. B: Condens. Matter Mater. Phys.* **2013**, *88*, 195313.
(45) Zhao, W.; Ghorannevis, Z.; Amara, K. K.; Pang, J. R.; Toh, M.; Zhang, X.; Kloc, C.; Tan, P. H.; Eda, G. *Nanoscale* **2013**, *5*, 9677.
(46) Terrones, H.; Corro, E. D.; Feng, S.; Poumirol, J. M.; Rhodes, D.; Smirnov, D.; Pradhan, N. R.; Lin, Z.; Nguyen, M. A. T.; Elías, A. L.; Mallouk, T. E.; Balicas, L.; Pimenta, M. A.; Terrones, M. *Sci. Rep.* **2014**, *4*, 4215.
(47) O'Brien, M.; McEvoy, N.; Hanlon, D.; Hallam, T.; Coleman, J. N.; Duesberg, G. S. *Sci. Rep.* **2016**, *6*, 19476.
(48) Damen, T. C.; Porto, S. P. S.; Tell, B. *Phys. Rev.* **1966**, *142*, 570.
(49) Zhao, Y.; Luo, X.; Li, H.; Zhang, J.; Araujo, P. T.; Gan, C. K.; Wu, J.; Zhang, H.; Quek, S. Y.; Dresselhaus, M. S.; Xiong, Q. *Nano Lett.* **2013**, *13*, 1007.
(50) Yan, T. F.; Qiao, X. F.; Liu, X. N.; Tan, P. H.; Zhang, X. H. *Appl. Phys. Lett.* **2014**, *105*, 101901.
(51) Tongay, S.; Suh, J.; Ataca, C.; Fan, W.; Luce, A.; Kang, J. S.; Liu, J.; Ko, C.; Raghunathanan, R.; Zhou, J.; Ogletree, F.; Li, J.; Grossman, J. C.; Wu, J. *Sci. Rep.* **2013**, *3*, 2657.
(52) Gutiérrez, H. R.; Perea-López, N.; Elías, A. L.; Berkdemir, A.; Wang, B.; Lv, R.; López-Urías, F.; Crespi, V. H.; Terrones, H.; Terrones, M. *Nano Lett.* **2013**, *13*, 3447.
(53) Wei-Chung, C.; Feldman, B. J. *Solid State Commun.* **1981**, *40*, 225.
(54) Tonndorf, P.; Schmidt, R.; Böttger, P.; Zhang, X.; Börner, J.; Liebig, A.; Albrecht, M.; Kloc, C.; Gordan, O.; Zahn, D. R. T.; Michaelis de Vasconcellos, S.; Bratschitsch, R. *Opt. Express* **2013**, *21*, 4908.
(55) Zeng, H.; Liu, G.-B.; Dai, J.; Yan, Y.; Zhu, B.; He, R.; Xie, L.; Xu, S.; Chen, X.; Yao, W.; Cui, X. *Sci. Rep.* **2013**, *3*, 1608.
(56) Chhowalla, M.; Shin, H. S.; Eda, G.; Li, L.-J.; Loh, K. P.; Zhang, H. *Nat. Chem.* **2013**, *5*, 263.
(57) Page, T. F. Silicon Carbide: Structure and Polytypic Transformations. In *The Physics and Chemistry of Carbides, Nitrides and Borides*; Freer, R, Ed.; Springer: Dordrecht, the Netherlands, 1990; pp 197.


DOI: 10.1021/jacs.6b12559
*J. Am. Chem. Soc.* 2017, 139, 3496−3504